

A variability-aware simulation and design workflow for wafer-scale, heterogeneously integrated lithium niobate modulators

P.Nenezic,^{1,2} E. Vissers,^{3,2} A. Moerman,^{3,2,4} L. Bogaert,^{3,2} S. Atzeni,^{3,2} X. Zheng,^{3,2} T. Vanackere,^{3,2} M. Niels,^{3,2} A. Papadopoulou,^{3,2} S. Uvin,^{3,2} P. De Heyn,² S. Saseendran,² M. Billet,^{3,2} and B. Kuyken^{3,2}

¹⁾*Department of Information Technology Photonics Research Group Ghent University–imec, 9052 Ghent, Belgium.*

²⁾*imec, Kapeldreef 75, 3001 Leuven, Belgium.*

³⁾*Department of Information Technology, Photonics Research Group, Ghent University–imec, 9052 Ghent, Belgium.*

⁴⁾*Department of Information Technology, IDLab, Ghent University–imec, 9052 Ghent, Belgium.*

(*Electronic mail: patrick.nenezic@ugent.be)

We present a variability-aware simulation framework for heterogeneously integrated lithium niobate traveling-wave modulators. The framework incorporates fabrication-variation data obtained from our dedicated pilot line and enables efficient optimisation of geometric parameters to ensure stable device performance across wafer-scale manufacturing. Using this methodology, we theoretically demonstrate that reliable wafer-scale integration of LN modulators on silicon photonics via micro-transfer printing is feasible and can be systematically engineered.

I. INTRODUCTION

The rapid, exponential growth of data traffic is driving power consumption in data centres to unsustainable levels. Silicon photonics (SiPho) platforms have enabled significantly higher data rates with greatly reduced energy requirements. Silicon photonic integrated circuits (Si-PICs) make it possible to densely integrate complex optical functions on a single silicon chip using standard CMOS fabrication processes, supporting high-volume, high-yield, and cost-effective manufacturing. However, emerging communication standards are now targeting baud rates beyond 200 GBd—levels that are difficult to attain with today’s silicon photonic modulators.

To overcome these limitations, several alternative electro-optic (EO) materials have been investigated, including BTO¹, organic materials², plasmonics³, and more recently lithium tantalate^{4,5}. Among these, thin-film lithium niobate (TFLN) stands out due to its relative maturity, its low loss and strong Pockels effect, with monolithic devices already exceeding 100 GHz bandwidth⁶. However, pure TFLN platforms lack integrated photodetectors and CMOS-compatible functionality. Heterogeneous TFLN-on-silicon integration addresses this gap by combining EO modulation performance of TFLN with the mature, high-yield components of silicon photonics and CMOS electronics, enabling a more complete platform.

As lithium-niobate (LN) modulator technologies continue to mature, an important question is whether this material platform—particularly in its heterogeneously integrated form—can be scaled to support wafer-level device manufacturing. Several efforts toward such scalability have emerged, primarily relying on wafer bonding^{7–9} or micro-transfer printing (MTP)^{10–12}. While these studies demonstrate the feasibility of wafer-scale processing, they do not address the design constraints needed to ensure that modulators maintain their target performance specifications under high-yield wafer-scale fabrication. Achieving robust, reproducible device performance at wafer scale demands modulator designs

that can tolerate fabrication-induced variations. Although variability-aware design methodologies have been explored for silicon photonic circuit components^{13–15}, they have not been extended to traveling-wave electro-optic modulators, and in particular not to heterogeneously integrated LN modulators.

First, this work proposes two modulation architectures compatible with wafer-scale MTP and provides a comparative analysis. Furthermore, it establishes a unified EO design framework that allows for the efficient optimisation of heterogeneously integrated LN modulators while explicitly incorporating fabrication-induced variability into the design process. By using fabrication variation data from our TRANSVERSE pilot line, we demonstrate that, with a rigorous and systematic design methodology, the wafer-scale integration of LN modulators on silicon photonics using micro-transfer printing is feasible.

In Section 2, based on our recent results of micro-transfer printed 200 mm silicon photonics wafer, proposes two design architectures which act as the example of our analysis. Section 3, with the help of a created simulation database, analyses the influence of geometric parameters on device performance. Finally, Section 4 introduces a new design framework and explains a statistical optimisation approach, which incorporates fabrication variations into the optimisation. Although the proposed framework is demonstrated with micro-transfer printing, it is equally applicable to other heterogeneous integration approaches such as die to wafer bonding. Furthermore, due to similarities in material properties, the presented methodology is also valid for heterogeneous lithium tantalate traveling wave modulators.

II. CURRENT STATE OF MICRO TRANSFER PRINTING AT WAFER SCALE AND PROPOSED DEVICE STACKS

Recently, in our other work we demonstrated reliable MTP of LN waveguide-based modulators onto a full 200 mm SiPho

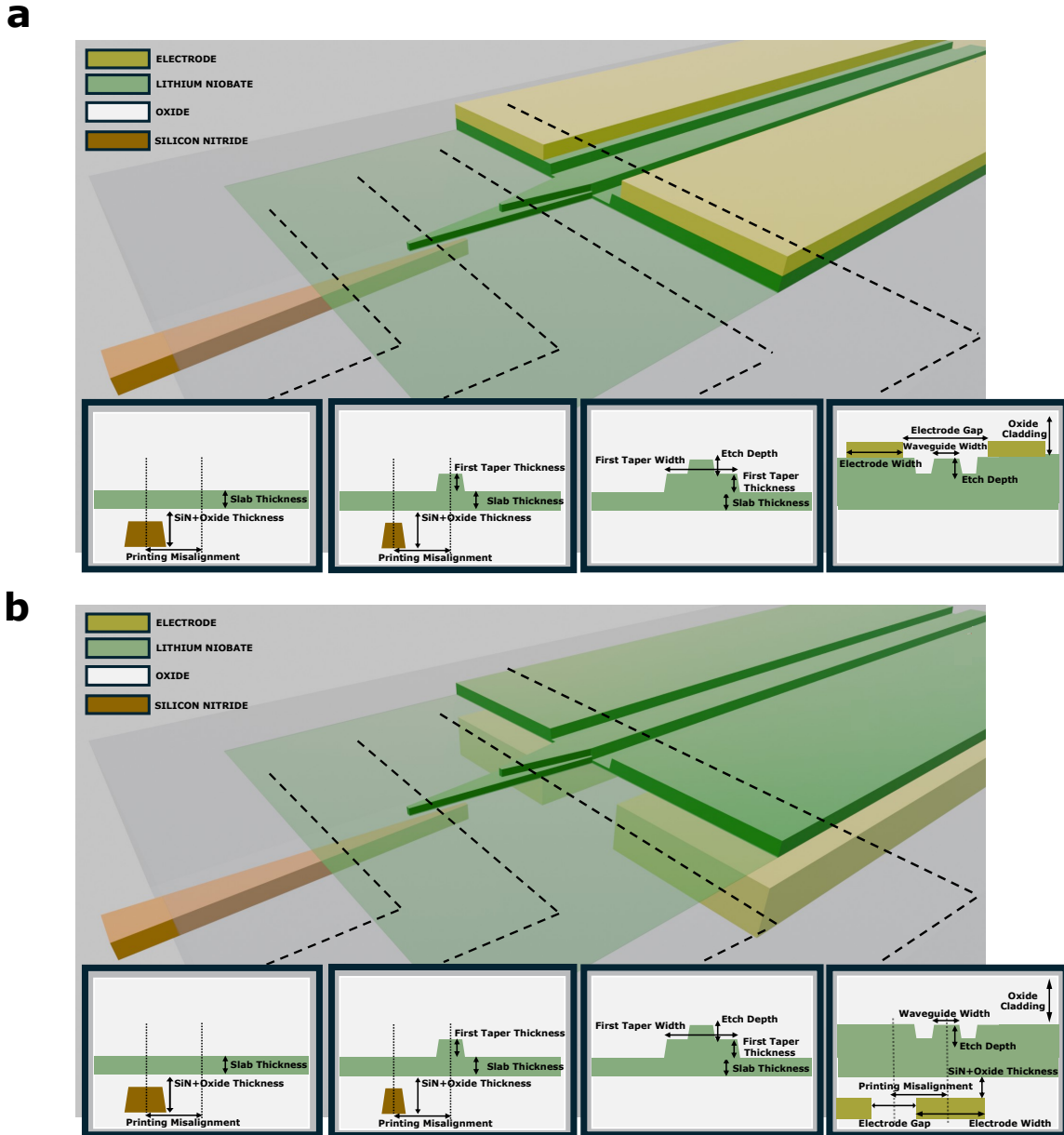


FIG. 1. (a) Schematic of the top electrode design. Metal electrodes are fabricated on the lithium niobate prior to integration onto the silicon nitride target wafer. This approach prevents the accumulation of alignment errors between the lithium niobate placement and the electrode definition, which can occur in post-processing metallisation schemes. Light is coupled from the target wafer into the lithium niobate waveguide via a two-layer adiabatic taper, minimising optical losses. (b) Schematic of the bottom electrode design. Metal electrodes are embedded in the target wafer, allowing an unmetallised lithium niobate layer to be integrated. This eliminates the need for post-processing metallisation and, similarly to the top electrode configuration, avoids cumulative alignment errors. The same tapering approach is applied as in the top electrode design.

wafer. However, performance limitations arise from the use of hybrid SiN/LN optical modes. To achieve improved performance in next-generation modulators, we propose two device architectures, as show in Fig. 1.

First, to enhance the EO efficiency of heterogeneously integrated LN modulators, we replace hybrid confinement in SiN/LN structure with full mode confinement in LN. This

would allow the optical mode to have a greater fraction inside the EO material than in hybrid architectures, thus experiencing a stronger electro-optic interaction. In order to achieve full coupling into LN waveguide, light is coupled from the silicon nitride, located in the target wafer, into the micro-transfer printed lithium niobate waveguide via multi-layer adiabatic waveguide tapering as shown in both Fig 1.a and Fig 1.b In

Fig 1.a, i.e. top electrode configuration, metallisation of the modulator is performed on the lithium niobate before integration. Contrary to the post-metallisation schemes, the metal is not defined with respect to the target wafer but with respect to the LN waveguide. This ensures printing misalignment of the lithium niobate is not added to the metal misalignment as it would with post-printing metallisation. This represents a second key difference compared to the method reported by in our other work. It is worth noting that a post-metallisation step may still be required for metal routing and bondpads definition. However, this step imposes less stringent alignment requirements, as the metal is located far from the modulation region and optical transitions. In Fig. 1.b the modulating section is different: the electrode is buried into the target wafer, meaning that once the lithium niobate structure is printed, no metallisation is required. This configuration, i.e. bottom electrode has not yet been widely adopted, although it has been proposed in literature as an alternative to the more standard approaches with post-processing metallisation^{16–18}. A great advantage of such configuration is that the metallisation can take place in a CMOS environment, consequently reducing overhead of back-end processing of heterogeneous integration, let it be micro-transfer printing or wafer bonding. Furthermore, it eliminates cumulative alignment errors due to LN integration and electrode lithography.

To evaluate the performance of the two proposed architectures, an extensive device performance database was created by simulating tens of thousands of parameter combinations. Various software tools were then used to extract the corresponding performance metrics, including $V_{\pi}L$, optical propagation loss in the modulating section, tapering loss, and several RF parameters, enabling the determination of the 3 dB bandwidth for each simulated device. The investigated parameters are denoted in the cross sections of Fig 1. In this paper, we limit the analysis to an optical wavelength of 1310 nm and assume copper as the metal layer, with material properties fixed to intrinsic ones of bulk copper. In addition, a GSGSG (ground-signal-ground-signal-ground) electrode structure on X-cut LN is adopted for both architectures. It is important to note that these assumptions do not compromise the generality of the proposed method, as variations in these parameters would simply extend the explored parameter space. In particular, we considered only parameters that can be directly tuned within our process flow or within the fabrication processes of our partners. Therefore, the ranges of the geometries are all defined within a realistic, fabricable range. It follows that the set of simulated geometry combinations is closely grounded in realistic design rules and includes structures that are compatible with fabrication in our dedicated pilot line. Additional information on figure of merits, theory, and simulation approaches for data collection can be found in the Supplementary Material.

III. GLOBAL CORRELATION AND SOBOLEV VARIANCE ANALYSIS

Once the device performance database has been established, the focus shifts to the identification of optimal design configurations. This requires a systematic assessment of how geometric parameters impact device performance across the dataset. To this end, we employ complementary sensitivity analysis techniques, including Pearson and Spearman correlations and Sobol variance decomposition. Correlation measures the direction of the output performance metric with respect to a single geometric parameter change, i.e. how changing a geometry parameter improves or worsens the performance metric¹⁹. On the other hand Sobol indices quantify how much of the total variance of the performance metric is explained by individual parameters (first-order S_1) and by their pairwise interactions (second-order S_2)²⁰. Second-order Sobol interactions especially give valuable insight as they show nonlinear, co-dependent effect of geometry variable pairs with respect to the performance metric. As correlation analyses cannot capture interactions between parameters and Sobol indices do not convey information on trend direction, the two approaches provide complementary insights. The correlation between device geometries and device performance is reported in Fig. 2 for both top and bottom electrode configurations, together with the most significant pairwise geometric interactions that non-additively affect the output performance, as identified by second-order Sobol indices. Details of these statistical tools and our data extraction methods can be found in the Supplementary material.

A. Top electrode configuration

This paragraph highlights the relationship between device performance and geometrical parameters for top electrode configuration. As shown in panel a of Fig. 2, the correlation analysis identifies the Electrode gap (g_{el}) as the most influential parameter affecting the electro-optic figure of merit $V_{\pi}L$. g_{el} shows a strong, directly proportional and linear relationship with $V_{\pi}L$: the smaller the gap the smaller the $V_{\pi}L$ of a modulator. Etch depth (d_{etch}) shows a weaker but still proportional and linear correlation, while Waveguide Width (w_{wg}) shows a negative, linear correlation.

Propagation loss exhibits qualitatively different and mostly opposite behaviour. Correlation shows that loss decreases monotonically with increasing g_{el} and d_{etch} . This relates accordingly to the expected physical behaviour: the farther the electrode is from the waveguide, the lower the metal-induced optical absorption becomes. Additionally, increasing the d_{etch} shifts the optical mode downward, further distancing it from the electrodes. Furthermore, Sobol analysis reveals that dominant contributions arise also from nonlinear/non-additive geometry parameter interactions. To understand what this means let us look at an additive and a non-additive interaction. An example for simple additive interaction is the one between d_{etch} and w_{wg} . Changing the d_{etch} primarily shifts the optical mode distribution vertically, whereas adjusting the

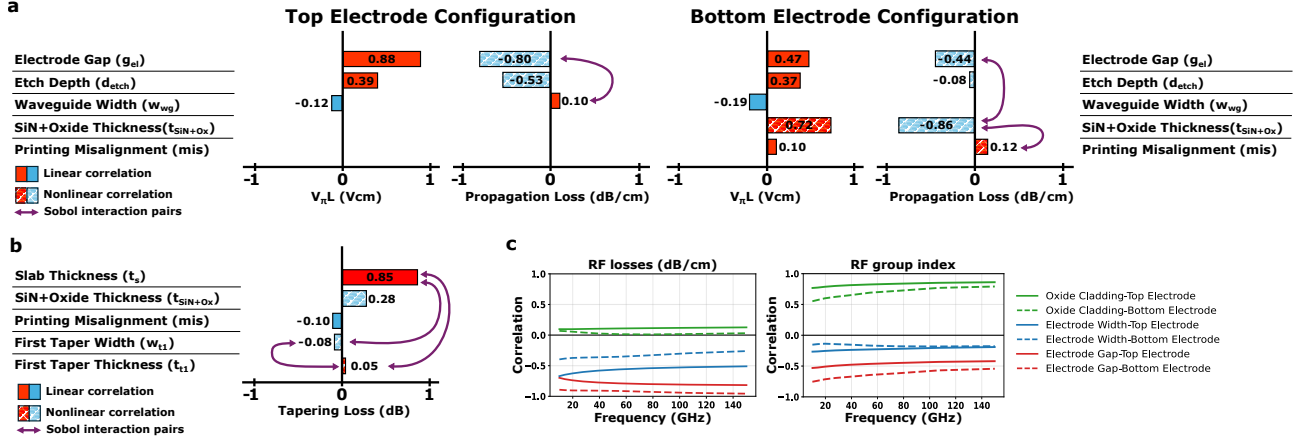


FIG. 2. (a) Influence of geometrical parameters on $V_{\pi}L$ and optical propagation loss for the top electrode configuration. The bar plot indicates linear (solid) and nonlinear (striped) correlations, while the purple arrows denote pairwise interactions. (b) Influence of geometrical parameters on $V_{\pi}L$ and optical propagation loss for the bottom electrode configuration. (c) Influence on geometrical parameters on tapering loss. Equal results for both top and bottom electrode configurations. (d) Influence of geometrical parameters on RF losses and RF group index.

w_{wg} predominantly modifies its lateral confinement. Because these two geometric parameters influence orthogonal aspects of the mode profile, their effects on optical propagation loss are largely independent. As a result, their individual contributions to the loss can be treated separately, and the total effect can be approximated as the sum of the two. In contrast, the interaction between w_{wg} and g_{el} constitutes a nonlinear, strongly second-order effect. When the g_{el} is small, even a modest change in w_{wg} can produce a disproportionately large change in propagation loss, owing to the increased sensitivity of the optical mode to lateral confinement near the metal boundary. The same magnitude of width variation leads to a much weaker loss change when the electrode gap is large. In this case, the influence of one geometric parameter on device performance directly depends on the value of another, indicating a genuine nonlinear interaction rather than an additive combination of independent effects. Such nonlinearly interacting parameter pairs are denoted as Sobol interaction pairs with purple arrows in Fig 2.

For $V_{\pi}L$ and propagation loss, Printing misalignment (mis) has no effect on the system as the light is fully coupled into the LN in the modulating section. The realistically possible offset of electrodes is small if metallisation happens with a high precision lithography tool (which was assumed in the database creation), thus having almost no effect on device performance.

In addition to metal-induced optical losses, device performance in terms of optical losses depends on how efficiently light is coupled from the SiN waveguide to the LN waveguide. This contribution is referred to as tapering loss in the following discussion. As reported in Fig. 2.c, tapering loss is dominated by t_s , which exhibits a very strong and monotonic positive relationship. t_{t1} and t_{SiN+Ox} have a weaker, positive, nonlinear correlation on tapering loss, while mis and w_{t1} show a negative correlation. There is a very strong Sobol interaction

between the t_s and the t_{t1} and weaker ones between w_{t1} - t_s and between w_{t1} - t_{t1} . In conclusion tapering loss can be controlled the most by controlling the t_s with the t_{SiN+Ox} , while also co-optimising t_{t1} , w_{t1} with the t_s .

The RF losses (in dB/cm) and RF group index ($n_{g,RF}$) are mainly governed by three geometry parameters: g_{el} , *Electrode width* and *Oxide cladding* and their correlations are RF frequency dependent. As shown on Fig 2.d, the RF losses are strongly and inversely correlated with g_{el} and *Electrode width*; i.e. the wider the g_{el} and larger the *width*, the lower the RF losses will be. The thickness of the *Oxide cladding* on top of the electrode and lithium niobate only weakly affects the RF losses. However, *Oxide cladding* strongly and positively influences the group index, as reported in Fig. 2d. In addition, its effect increases with frequency. In physical context this means that *Oxide cladding* slows the traveling RF wave down by increasing the group index and it increasingly does so at higher frequencies. Similarly to the RF losses, g_{el} and *Electrode width* are inversely correlated to group index. Sobol analysis shows that, for both RF losses and group index, there is no significant interplay between the geometrical parameters; therefore, they affect device performance independently.

B. Bottom electrode configuration

In the bottom electrode configuration, the correlation dynamics of $V_{\pi}L$ and propagation losses differ significantly from those of the top electrode configuration, as shown in Fig. 2a. For $V_{\pi}L$, both the g_{el} , d_{etch} and t_{SiN+Ox} are all strongly correlated parameters, with the latter exhibiting the strongest influence. Increasing any of these geometrical parameters results in a higher $V_{\pi}L$, and thus a deterioration in device performance. Furthermore, t_{SiN+Ox} correlates with $V_{\pi}L$ in a non-

linear fashion. This is due to the fact that the density of electric field lines overlapping with LN drops nonlinearly if the vertical distance between the electrode and LN increases. Although more parameters influence $V_\pi L$, they affect it independently, similarly to the top electrode configuration.

The correlation analysis of propagation loss reveals that t_{SiN+Ox} , which has no influence in the top electrode configuration, exhibits the strongest (nonlinear) correlation in the bottom electrode configuration. Its impact is nearly twice that of the electrode gap, highlighting this parameter as the dominant factor governing propagation loss. Furthermore, Sobol analysis shows a strict interaction between the two, meaning that they reinforce each others effect. d_{etch} is considerably less influential for bottom-electrode than for the top electrode configuration. Since the buried electrodes are laterally farther from the waveguide, the EO overlap is less affected by etch depth. Instead, it is more strongly governed by the oxide thickness separating the electrodes from the lithium niobate.

Tapering loss correlations are exactly the same as in the top electrode configuration, as in both configurations the metals are introduced once all the light is coupled into the LN waveguide.

Regarding RF properties, the correlating geometry parameters and trends are similar as for top electrodes. The correlation strength differs though, which can be attributed to the different location of the buried electrode in the stack. For example, the correlation between oxide cladding and the RF group index $n_{g,RF}$ is weaker in the bottom electrode configuration than in the top electrode case, as the electrodes are positioned significantly farther from the top cladding.

C. Summary

The performed analysis shows that device performance is governed by the simultaneous presence of linear, nonlinear, and interaction effects among multiple geometric parameters, thereby rendering the optimisation of device performance a highly non-trivial and complex task. In addition, the performance metrics were expressed as length-independent figures of merit. However, when the device length is also considered as a design parameter, it introduces an additional degree of freedom, thereby affecting the overall device performance and further increasing the complexity of the optimisation problem. Indeed, the longer the modulator, the lower the V_π , but the higher the propagation loss, as well as the RF losses. In addition, a longer device makes the matching between RF and optical group indices more difficult, thus leading to a reduction of the 3 dB bandwidth.

These trade-offs and the complexity of geometric parameter effects, further aggravated by pairwise parameter interactions, shows the individual optimisation of parameters is far from optimal, particularly in the bottom-electrode configuration. This leads to the need to co-optimize parameters such that V_π , loss, and bandwidth of a modulator are optimised simultaneously, without requiring iterative optimisation of the device for individual performance metrics. In case fabrication variations are also introduced, the need for a unified and

comprehensive device optimisation framework becomes even more pronounced. In the following section a unified optimisation method is proposed. This method finds the ideal modulator designs for all desired performance metrics at once while also taking into account fabrication variations.

IV. UNIFIED, FABRICATION AWARE OPTIMISATION METHOD

The results of the multidimensional simulation sweeps are stored using the Xarray library in Python. Xarray is an open-source Python package that provides data structures and analytical tools for working with multidimensional labeled arrays, enabling efficient storage, slicing, and interpolation of large scientific datasets²¹. Because the database grids are sufficiently dense in all design dimensions, performance metrics can be evaluated continuously across the full parameter space via interpolation. For any given device stack, the interpolated dataset can be visualized as a three-dimensional projection in performance space, where the x,y and z coordinates correspond to the half-wave voltage V_π , the optical insertion loss, and the RF bandwidth. Such a projected 'cloud' for the bottom electrode configuration is shown in Fig.3. Here, given a modulator length L , V_π refers to the half-wave voltage in a push-pull amplitude modulation configuration, the total insertion loss is given by the propagation loss times L plus twice the tapering loss, and the bandwidth corresponds to the electro-optic-electric (EOE) 3dB bandwidth. Since these metrics depend on the modulator length, varying the length results in a change and translation of the cloud in the performance space.

Once the database has been generated and interpolated, and the target device performance has been defined, the method can be applied not only to identify geometry parameters that achieve the desired performance, but also to determine parameter sets that are robust against unavoidable variations arising from standard fabrication tolerances. As an example, in our micro-transfer printed wafer-scale demonstrations we observed noticeable device-to-device performance variations across the wafer. Therefore, accounting for process variations in the optimisation routine is crucial when the target performance is required not only at the die level (i.e., for a "hero device"), but also across wafer-scale manufacturing.

Because the database is interpolated and effectively continuous, it is well suited for Monte Carlo analysis. Random perturbations can be drawn from the experimentally measured fabrication-distribution ranges, and each sample can be evaluated by direct lookup rather than by performing new simulations. This approach dramatically reduces the computational cost: a Monte Carlo analysis with 10 000 samples can be completed in only a few minutes.

To highlight the importance of co-optimising performance metrics under fabrication tolerance conditions, two bottom electrode, 7 mm-long modulator designs, denoted as A and B, are evaluated under identical fabrication variation ranges. The results of the Monte Carlo analysis are reported in Fig. 4. While the same evaluation can also be applied to top electrode configurations, the bottom electrode architecture is se-

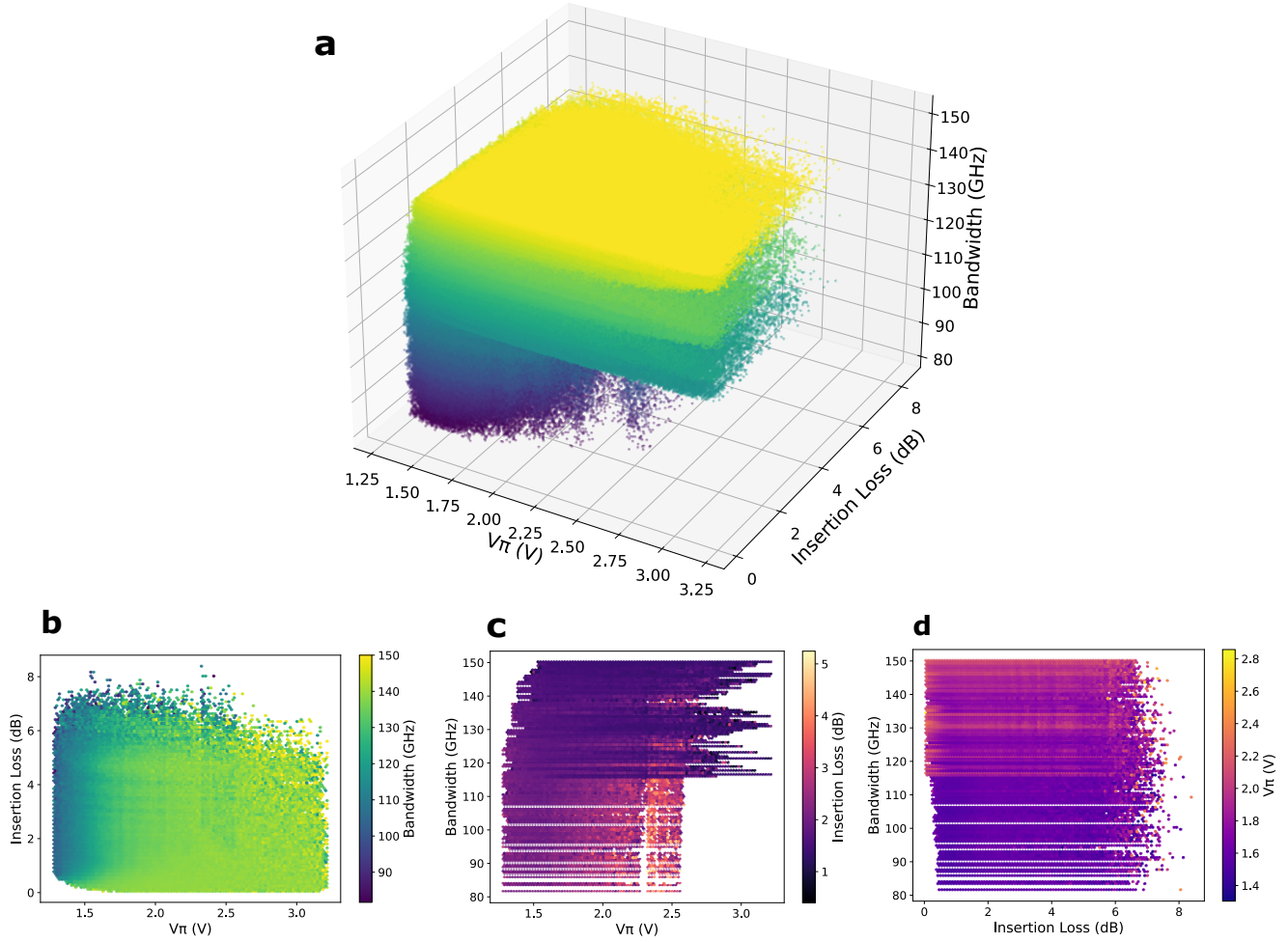


FIG. 3. (a) Three dimensional device performance projection of the XArray database for 7mm long bottom electrode configurations, with GSGSG electrode placing. By varying the modulator length, the cloud of designs is shifted in this 3 dimensional space. (b) A 2 dimensional representation of the cloud presenting the insertion loss- V_{π} slice. (c) A 2 dimensional representation of the cloud presenting the bandwidth- V_{π} slice. (d) A 2 dimensional representation of the cloud presenting the bandwidth-insertion loss slice.

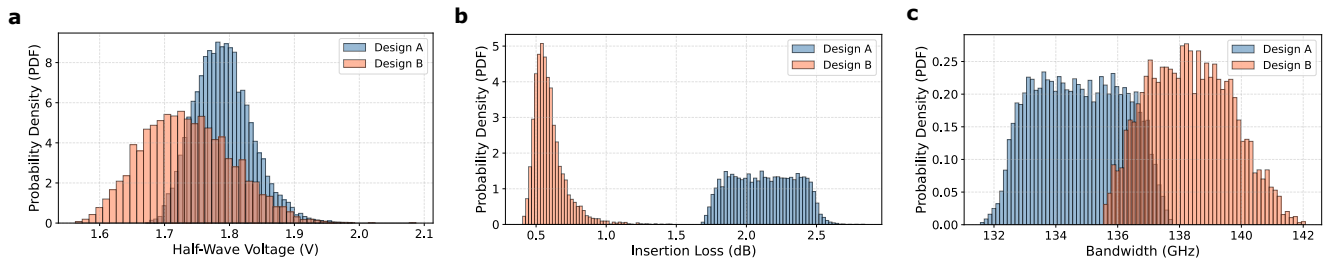


FIG. 4. Performance metric comparison of two bottom electrode designs (probability density function versus respective performance metric). (a) The designs have very similar nominal V_{π} values but Design A is less sensitive to fabrication variations. (b) When looking at insertion loss, Design A has much lower losses and is more robust to variations. (c) Both designs have similar fabrication sensitivity to bandwidth, with Design B having a slightly higher nominal bandwidth.

lected here as a representative example. Taking into account only the nominal V_π value, 1.79 V for A and 1.73 V for B, it would appear that two designs exhibit nearly identical performance. Furthermore, although both designs demonstrate robust behaviour under fabrication variations, design A exhibits a smaller performance spread, indicating superior stability. However, when insertion loss and bandwidth are considered simultaneously, Design B offers a better overall performance trade-off: it exhibits much lower insertion loss with reduced variability and a slightly higher bandwidth than Design A. This example highlights the importance of evaluating fabrication variations as well as all performance metrics together in a multidimensional framework rather than relying on any single metric.

These observations underscore the need for an automated method to identify geometries that optimally satisfy the target values for V_π , insertion loss, and bandwidth, while simultaneously maximising robustness against fabrication variations. The method is described in detail in the following paragraph.

Let \mathbf{x} denote the vector containing the nominal geometry variables of the desired modulator design. However in practice the fabricated device may deviate from these nominal values. Therefore, the geometry vector including fabrication variations can be written as

$$\tilde{\mathbf{X}} = \begin{pmatrix} \text{Parameter}_1 + \Delta_1 \\ \text{Parameter}_2 + \Delta_2 \\ \text{Parameter}_3 + \Delta_3 \\ \vdots \\ \text{Parameter}_i + \Delta_i \end{pmatrix},$$

where Δ_i represents the fabrication-induced deviation of Parameter i . Each deviation has a variation range and follows a probability distribution. These have been obtained from our value chain partners and our own TRANSVERSE pilot production line. For example, the MTP process exhibits a quasi-Gaussian misalignment distribution with a range of ± 500 nm. This experimentally obtained distributions are embedded directly into the model, with only the nominal vector \mathbf{x} being adjusted during optimisation, whereas the distributions of Δ_i remain fixed.

With the probability distributions and ranges defined, a Monte Carlo analysis with N samples can be performed. Then, for a given modulator length, the empirical expected value of each metric m is computed as

$$\hat{\mathbb{E}}[m] = \frac{1}{N} \sum_{k=1}^N m(\tilde{\mathbf{X}}^{(k)}), \quad m \in \{V_\pi, \text{Loss}, \text{BW}_{3\text{dB}}\}. \quad (1)$$

The expected value represents the average performance of the modulator under fabrication variations. It therefore reflects the typical (mean) metric value one can expect from real fabricated devices of the chosen geometry.

We estimate the variance of a metric $m(\tilde{\mathbf{X}})$ under fabrication variations by

$$\widehat{\text{Var}}[m] = \frac{1}{N-1} \sum_{k=1}^N (m(\tilde{\mathbf{X}}) - \hat{\mathbb{E}}[m])^2.$$

The squared deviations quantify how strongly m fluctuates around its mean, with large outliers penalised more heavily and such that contributions from positive and negative deviations do not cancel each other out. The division by $N-1$ (Bessel's correction) accounts for the fact that the sample mean $\hat{\mathbb{E}}[m]$ is estimated from the same data, using up one degree of freedom; this yields an unbiased estimate of the true variance and prevents systematic underestimation for finite N . Overall, a low variance indicates that the metric is stable, i.e., robust to parameter deviations, whereas a high variance signals that small fabrication errors can cause large performance fluctuations. Thus, variance directly measures fabrication sensitivity. It is worth noting that the relative effect of geometry parameters on the device may differ from the relative correlations observed in Section 2. In that case, the full simulation space was analysed, highlighting global trends, whereas here the fabrication variation ranges and their associated probability distributions determine the actual magnitude of their impact on the performance metrics.

To jointly meet desired performance targets while ensuring robustness to fabrication variations, the following function is defined:

$$J(\mathbf{x}) = \sum_{m \in \{V_\pi, \text{Loss}, \text{BW}_{3\text{dB}}\}} \left[\alpha_m \left(\frac{\hat{\mathbb{E}}[m(\tilde{\mathbf{X}})] - m_{\text{target}}}{R_m} \right)^2 + \gamma_m \left(\frac{\widehat{\text{Var}}[m(\tilde{\mathbf{X}})]}{R_m^2} \right) \right]. \quad (2)$$

Here, m_{target} denotes the desired value of metric m , and R_m is the total range of the given metric within the database. Normalizing the mean-deviation term by R_m and the variance term by R_m^2 ensures that all three metrics contribute to the objective in a dimensionless and comparable manner, regardless of their physical units or numerical ranges.

The coefficients α_m and γ_m control the relative importance

assigned to performance accuracy and fabrication robustness, respectively. To separate these two roles cleanly, we introduce *priority weights* w_m that express the designer-selected importance of matching the target value for metric m , and *robustness weights* c_m that specify how strongly deviations due to fabrication variations should be penalised. These weights define

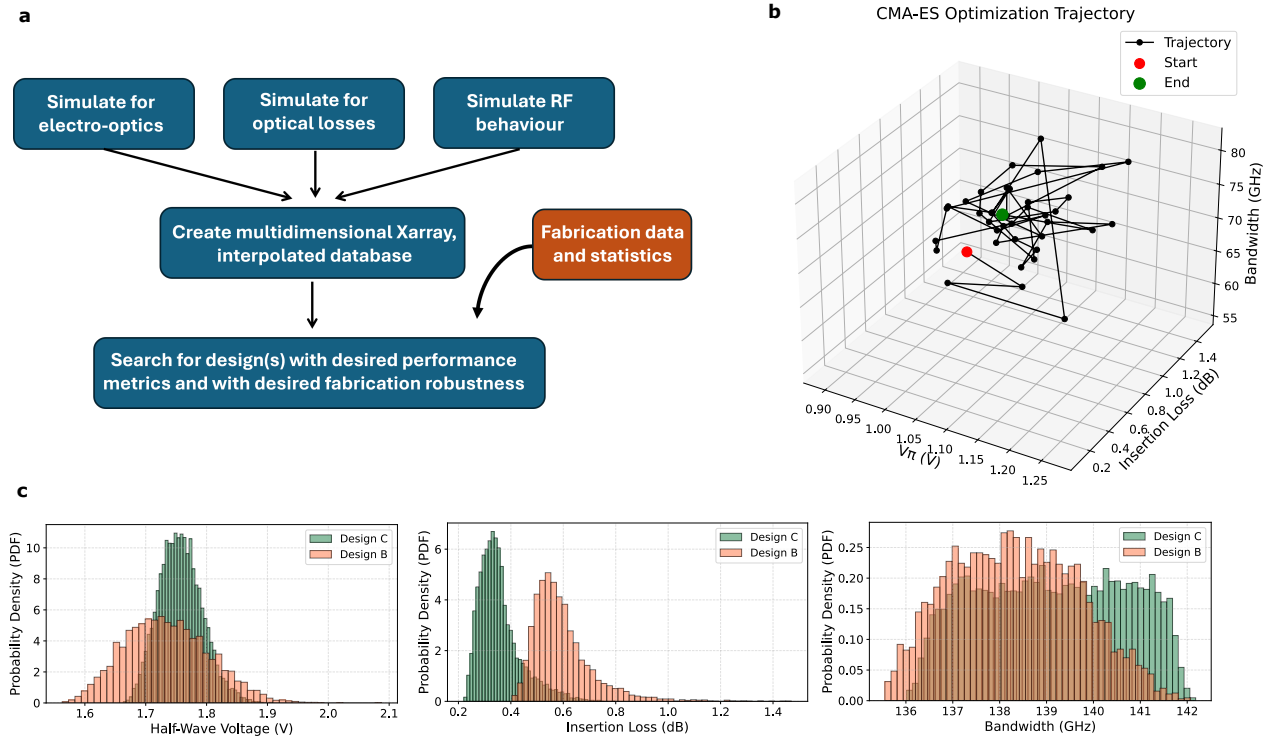


FIG. 5. (a) Schematic optimisation flow of our design approach. (b) CMA-ES optimisation trajectory. Each point is the best solution of a generation of statistical simulations. The simulations space around the performance metric targets are explored from generation to generation until reaching the best design. (c) By optimising for the target metrics of Design B the algorithm finds Design C. It is in more robust to fabrication variations than Design B.

TABLE I. Performance metrics of three modulators with bottom electrode configurations, designed by the presented methodology.

Case	Modulator Length (mm)	V_{π} (V)	Insertion loss (dB)	Bandwidth (GHz)	Notes
1	7	1.78 ± 0.04	0.3 ± 0.02	139 ± 2	BiCMOS driving
2	5	2.25 ± 0.16	0.38 ± 0.01	150+	BiCMOS driving, smaller devices
3	12	1.025 ± 0.025	0.82 ± 0.1	95 ± 3	CMOS driving, low V_{π} variance

the cost coefficients as

$$\alpha_m = w_m, \quad \gamma_m = c_m \alpha_m. \quad (3)$$

This formulation ensures that, when w_m are chosen equal, all three target metrics are equally important to reach regardless of the difference in the physical range of the metrics. At the same time, the parameters c_m provide the flexibility to penalize fabrication sensitivity differently across the metrics (e.g. enforcing stricter robustness for insertion loss than for bandwidth). For a pre-set modulator length, and with the input of m_{target} , α_m and γ_m , the optimal device geometry can be found by minimizing $J(\mathbf{x})$. This is done with Covariance Matrix Adaptation Strategy (CMA-ES). CMA-ES is a gradient-free optimisation method that works by sampling many candidate designs, selecting the best ones, and then updating its search distribution to move towards better regions of the design space²². It adapts both the position and the shape of its search distribution, allowing it to efficiently explore complex and noisy objective landscapes such as the one analysed.

An example of such optimisation trajectory is shown in Fig. 5.b. By setting the performance targets in the algorithm to the means of Design B of Fig.4, we get a fully optimised geometry, Design C, as shown on Fig 5.c.

To demonstrate the effectiveness of the methodology, we investigated several configurations compatible with the processing workflow established in the Transverse pilot line and targeting specific performance metrics. In particular, the optimisation routine was applied to identify the parameters of heterogeneously integrated LN modulators that meet predefined targets, as detailed below. Case 1 is based on a standard modulator length, as reported in our other work, and aims at achieving low insertion loss, a half-wave voltage compatible with BiCMOS driving, and a high bandwidth exceeding 110 GHz. Case 2 targets a shorter device reaching an even higher bandwidth above 150 GHz, while minimising insertion loss and maintaining V_{π} compatibility with BiCMOS driving. Case 3 focuses on achieving a V_{π} compatible with CMOS driving,

while optimising both bandwidth and insertion loss. As reported in Table 1, the proposed method enables the identification of fabrication tolerant designs that fulfil the specified performance metrics.

V. DISCUSSION AND CONCLUSION

In this work, we presented a variability-aware design and optimisation framework for heterogeneously integrated lithium niobate traveling-wave modulators targeting wafer-scale fabrication. Through a comparative analysis of a top- and bottom-electrode architectures, we identified the dominant geometric parameters governing electro-optic efficiency, optical propagation loss, RF performance, and tapering loss, as well as their nonlinear interaction effects. The combination of global correlation analysis and Sobol variance decomposition revealed that, while certain performance metrics are primarily driven by single-parameter variations, others depend strongly on second-order interactions. Furthermore, some design parameters have opposite effect on different performance metrics, introducing tradeoffs. These findings emphasize the limitations of sequential or single-metric design approaches and motivate the need for simultaneous multi-parameter co-optimisation.

Building on this analysis, we introduced a statistics based optimisation strategy that explicitly incorporates fabrication-induced variations into the design loop. By combining Monte Carlo sampling with a unified cost function that penalises both deviations from the target performance and sensitivity to geometric fluctuations, and by solving the resulting optimisation problem using the gradient-free CMA-ES algorithm, we demonstrate the ability to identify modulator geometries that, for a given device length, simultaneously achieve the desired V_π , insertion loss, and bandwidth, while exhibiting improved robustness. Case studies illustrate that designs with similar nominal performance can exhibit substantially different variability behavior, highlighting the importance of robustness-aware optimisation in the context of wafer-scale manufacturing.

The proposed framework is grounded in experimentally measured fabrication statistics obtained from a MTP pilot line, including realistic parameter distributions that are directly embedded in both the performance model and the function $J(\mathbf{x})$. Consequently, the optimisation results reflect the current state of the fabrication process rather than idealised or assumed tolerances. The optimized geometries obtained within this framework define concrete, pilot-line-compatible designs that can be fabricated and evaluated experimentally.

Future work will extend the present simulation database beyond 1310 nm to other wavelengths, as well as to other material stacks and alternative metallisation schemes. Furthermore, advanced traveling-wave electrode geometries, including T-shaped electrodes, will be incorporated to enable longer modulator devices with reduced RF loss and bandwidths exceeding 110 GHz, while maintaining compatibility with wafer-scale heterogeneous integration flows.

Rather than replacing experimental validation, the proposed

framework is intended to operate within an iterative design–fabrication–verification loop. The sensitivity and interaction information extracted from the model enables to make targeted, low-dimensional design-of-experiments focused on a limited set of high-impact process parameters. Wafer-level measurement data can then be used to verify model predictions, monitor process evolution, and update the statistical distributions used in subsequent optimisation cycles. This iterative approach supports progressive refinement of both device designs and process assumptions, facilitating convergence toward stable and reproducible modulator performance under pilot-line manufacturing conditions.

From a broader system-level perspective, no single modulator design is universally optimal, as different applications impose distinct priorities on device length, insertion loss, bandwidth, drive voltage, and robustness. By explicitly navigating these trade-offs under realistic fabrication constraints, the proposed framework enables the deliberate tailoring of modulator designs to specific application requirements and customer needs, rather than forcing convergence to a single, ideal design. As heterogeneous photonic integration moves toward high-volume manufacturing, such variability-aware design methodologies will be essential for bridging the gap between state-of-the-art single-device performance and reproducible, high-yield production.

ACKNOWLEDGMENTS

We would like to thank Prof. Peter Bienstman for his valuable input. The authors would like to also thank the imec-Leuven teams providing the silicon and silicon nitride photonic waveguide circuits for our pilot line. The research has been made possible by FWO and F.R.S.-FNRS under the Excellence of Science (EOS) program (40007560). The work has been supported by The Dutch National Growth Fund PhotonDelta, CHIPS-JU PhotonixFAB (101111896) and STARLIGHT(101194170).

- ¹D. Chelladurai, M. Kohli, J. Winiger, D. Moor, A. Messner, Y. Fedoryshyn, M. Eleraky, Y. Liu, H. Wang, and J. Leuthold, “Barium titanate and lithium niobate permittivity and Pockels coefficients from megahertz to sub-terahertz frequencies,” *Nature Materials* **24**, 868–875 (2025).
- ²S. Wolf, H. Zwickel, W. Hartmann, M. Laueremann, Y. Kutuvantavida, C. Kieninger, L. Altenhain, R. Schmid, J. Luo, A. K.-Y. Jen, S. Randel, W. Freude, and C. Koos, “Silicon-Organic Hybrid (SOH) Mach-Zehnder Modulators for 100 Gbit/s on-off Keying,” *Scientific Reports* **8**, 2598 (2018).
- ³C. Haffner, W. Heni, Y. Fedoryshyn, J. Niegemann, A. Melikyan, D. L. Elder, B. Baeuerle, Y. Salamin, A. Josten, U. Koch, C. Hoessbacher, F. Ducry, L. Juchli, A. Emboras, D. Hillerkuss, M. Kohl, L. R. Dalton, C. Hafner, and J. Leuthold, “All-plasmonic Mach-Zehnder modulator enabling optical high-speed communication at the microscale,” *Nature Photonics* **9**, 525–528 (2015).
- ⁴C. Wang, Z. Li, J. Riemensberger, G. Lihachev, M. Churaev, W. Kao, X. Ji, J. Zhang, T. Blesin, A. Davydova, Y. Chen, K. Huang, X. Wang, X. Ou, and T. J. Kippenberg, “Lithium tantalate photonic integrated circuits for volume manufacturing,” *Nature* **629**, 784–790 (2024).
- ⁵M. Niels, T. Vanackere, E. Vissers, T. Zhai, P. Nenezic, J. Declercq, C. Bruynsteen, S. Niu, A. Moerman, O. Caytan, N. Singh, S. Lemey, X. Yin, S. Janssen, P. Verheyen, N. Singh, D. Bode, M. Davi, F. Ferraro, P. Absil, S. Balakrishnan, J. Van Campenhout, G. Roelkens, B. Kuyken,

- and M. Billet, "A high-speed heterogeneous lithium tantalate silicon photonics platform," *Nature Photonics* **20**, 225–231 (2026).
- ⁶D. Zhu, L. Shao, M. Yu, R. Cheng, B. Desiatov, C. J. Xin, Y. Hu, J. Holzgrafe, S. Ghosh, A. Shams-Ansari, E. Puma, N. Sinclair, C. Reimer, M. Zhang, and M. Lončar, "Integrated photonics on thin-film lithium niobate," *Advances in Optics and Photonics* **13**, 242–352 (2021).
- ⁷A. Rahman, F. Valdez, V. Mere, C. Op de Beeck, P. Wuytens, and S. Mookherjee, "Integration of Hybrid Thin-Film Lithium Niobate Electro-optic Modulators on a Wafer-scale Silicon Nitride Photonics Platform," *Journal of Lightwave Technology*, 1–11 (2025).
- ⁸M. Churaev, R. N. Wang, A. Riedhauser, V. Snigirev, T. Blésin, C. Möhl, M. H. Anderson, A. Siddharth, Y. Popoff, U. Drechsler, D. Caimi, S. Hönl, J. Riemensberger, J. Liu, P. Seidler, and T. J. Kippenberg, "A heterogeneously integrated lithium niobate-on-silicon nitride photonic platform," *Nature Communications* **14**, 3499 (2023).
- ⁹S. Ghosh, S. Yegnanarayanan, D. Kharas, M. Ricci, J. J. Plant, and P. W. Juodawlkis, "Wafer-scale heterogeneous integration of thin film lithium niobate on silicon-nitride photonic integrated circuits with low loss bonding interfaces," *Optics Express* **31**, 12005–12015 (2023).
- ¹⁰M. Niels, E. Vissers, T. Vanackere, A. Moerman, X. Zheng, X. Guo, P. Geerinck, E. Soltanian, J. Zhang, S. Janssen, P. Verheyen, N. Singh, D. Bode, M. Davi, F. Ferraro, P. Absil, S. Balakrishnan, J. Van Campenhout, S. Hänsch, H. Mai, N. Singh, G. Roelkens, S. Uvin, M. Billet, and B. Kuyken, "Wafer-Scale Integration of Lithium Niobate on a Silicon Photonics 200-mm Platform," in *2025 IEEE Photonics Conference (IPC)* (2025) pp. 1–2.
- ¹¹M. Niels, T. Vandekerckhove, L. De Jaeger, M. Billet, and B. Kuyken, "Advances in Micro-Transfer Printing of Lithium Niobate Thin-Films for Silicon Photonic Devices," *Nanophotonics* **15**, e70042 (2026), [_eprint: https://onlinelibrary.wiley.com/doi/pdf/10.1002/nap.2.70042](https://onlinelibrary.wiley.com/doi/pdf/10.1002/nap.2.70042).
- ¹²L. Lu, J. Su, Y. Yuan, Y. Dai, A. Sun, S. Ran, W. Gao, W. Liu, Y. Liu, J. Zhang, C. Zeng, B. Dong, Y. Li, N. Chi, J. Xia, J. Chen, and L. Zhou, "A Broadband Lithium Tantalate-on-Silicon Nitride Heterogeneous Modulator for Optical and Terahertz Communications and Radar Sensing," (2026), iSSN: 2693-5015.
- ¹³W. Bogaerts, Y. Xing, and U. Khan, "Layout-Aware Variability Analysis, Yield Prediction, and Optimization in Photonic Integrated Circuits," *IEEE Journal of Selected Topics in Quantum Electronics* **25**, 1–13 (2019).
- ¹⁴Z. Zhang, S. I. El-Henawy, R. Miller, and D. S. Boning, "Decomposed representation of S-parameters for silicon photonic variation analysis," in *Optical Modeling and Performance Predictions XI*, Vol. 11484 (SPIE, 2020) pp. 29–41.
- ¹⁵T. Ullrick, D. Spina, W. Bogaerts, and T. Dhaene, "Wideband parametric baseband macromodeling of linear and passive photonic circuits via complex vector fitting," *Scientific Reports* **13**, 15407 (2023).
- ¹⁶R. Safian, M. Teng, L. Zhuang, and S. Chakravarty, "Foundry-compatible thin film lithium niobate modulator with RF electrodes buried inside the silicon oxide layer of the SOI wafer," *Optics Express* **28**, 25843–25857 (2020).
- ¹⁷N. Boynton, H. Cai, M. Gehl, S. Arterburn, C. Dallo, A. Pomerene, A. Starbuck, D. Hood, D. C. Trotter, T. Friedmann, C. T. DeRose, and A. Lentine, "A heterogeneously integrated silicon photonic/lithium niobate travelling wave electro-optic modulator," *Optics Express* **28**, 1868–1884 (2020).
- ¹⁸M. Zhang, C. Wang, P. Kharel, D. Zhu, and M. Lončar, "Integrated lithium niobate electro-optic modulators: when performance meets scalability," *Optica* **8**, 652–667 (2021).
- ¹⁹J. Lee Rodgers and W. A. Nicewander, "Thirteen Ways to Look at the Correlation Coefficient," *The American Statistician* **42**, 59–66 (1988), [_eprint: https://doi.org/10.1080/00031305.1988.10475524](https://doi.org/10.1080/00031305.1988.10475524).
- ²⁰J. L. Hart, A. Alexanderian, and P. A. Gremaud, "Efficient Computation of Sobol' Indices for Stochastic Models," *SIAM Journal on Scientific Computing* **39**, A1514–A1530 (2017).
- ²¹S. Hoyer and J. Hamman, "xarray: N-D labeled Arrays and Datasets in Python," *Journal of Open Research Software* **5** (2017), 10.5334/jors.148.
- ²²M. Nomura, M. Shibata, and R. Hamano, "cmaes: A Simple yet Practical Python Library for CMA-ES," (2026), [arXiv:2402.01373 \[cs\]](https://arxiv.org/abs/2402.01373).
- ²³A. Honardoost, R. Safian, A. Rao, and S. Fathpour, "High-Speed Modeling of Ultracompact Electrooptic Modulators," *Journal of Lightwave Technology* **36**, 5893–5902 (2018).
- ²⁴M. Lin, Z. Li, A. Kotz, H. Larocque, N. Kuznetsov, J. Sun, Y. Zhang, S. Zheng, J. Riemensberger, C. Koos, and T. J. Kippenberg, "Copper damascene process-based high-performance thin-film lithium tantalate modulators," *Nature Communications* **17**, 3211 (2026).